◯ Discover

Research

Multimodal and multiscale investigation for the optimization of AlSi10Mg components made by powder bed fusion-laser beam

Flavio Cognigni[1] · Mirko Sgambetterra[2,3] · Guido Zucca[2] · Domenico Gentile[4] · Sara Ricci[3] · Gabriel Testa[3] · Gabriele Rizzi[5] · Marco Rossi[1]

© The Author(s) 2023   OPEN

Abstract
In recent years, there has been a growing interest in the use of additive manufacturing (AM) to fabricate metallic components with tailored microstructures and improved mechanical properties. One of the most promising techniques for the aerospace industry is powder bed fusion-laser beam (PBF-LB). This technique enables the creation of complex shapes and structures with high accuracy and repeatability, which is especially important for the aerospace industry where components require high precision and reliability. However, the impact of the PBF-LB process on microstructural features, such as the grain size distribution and porosity, remains an important area of research since it influences mechanical properties and performance of materials. In this study, a multimodal and multiscale correlative microscopy approach is used to investigate the microstructure of AlSi10Mg components made by PBF-LB. The study found that the correlative microscopy approach involving X-ray images with visual, chemical, and diffraction information coming from optical microscopy (OM), scanning electron microscopy (SEM) and electron backscatter diffraction (EBSD) is highly effective in reaching a more comprehensive understanding of the relationship between the fabrication process and the effective microstructure of PBF-LB fabricated components enabling the optimization of their performance for a wide range of applications.

Keywords Correlative microscopy · Additive manufacturing · Powder bed fusion-laser beam · Alloy · Electron backscatter diffraction · X-ray microscopy

1 Introduction

Additive manufacturing (AM) has revolutionized the way metallic components are fabricated. In recent years, there has been a growing interest in using AM techniques to fabricate metallic components with tailored microstructures and improved mechanical properties [1, 2]. One of the most promising AM techniques is powder bed fusion-laser beam (PBF-LB), broadly referred to as Selective Laser Melting (SLM), which enables the creation of complex shapes and structures with high accuracy and repeatability [3]. PBF-LB involves the use of a high-power laser to fuse metal powder into solid components. The process begins with the creation of a 3D model of the component using computer-aided design (CAD)

✉ Flavio Cognigni, flavio.cognigni@uniroma1.it; Mirko Sgambetterra, mirko.sgambetterra@aeronautica.difesa.it; Guido Zucca, guido.zucca@aeronautica.difesa.it; Domenico Gentile, domenico.gentile@unimol.it; Sara Ricci, sara.ricci@unicas.it; Gabriel Testa, gabriel.testa@unicas.it; Gabriele Rizzi, g.rizzi@beam-it.eu; Marco Rossi, marco.rossi@uniroma1.it | [1]Department of Basic and Applied Sciences for Engineering (SBAI), University of Rome La Sapienza, 00185 Rome, Italy. [2]Italian Air Force-Aeronautical and Space Test Division, 00040 Pomezia, RM, Italy. [3]University of Cassino and Southern Lazio, 03043 Cassino, FR, Italy. [4]Department of Medicine and Life Sciences "Vincenzo Tiberio", University of Molise, 86100 Campobasso, CB, Italy. [5]BEAMIT S.p.A, Strada Prinzera 17, 43045 Fornovo di Taro, PR, Italy.

software. The metal powder is then spread out in a thin layer on a build platform, and the laser beam is focused onto the powder, selectively melting it in a controlled manner to form the desired component layer by layer. The aerospace industry has been quick to recognize the potential benefits of PBF-LB, particularly in the fabrication of lightweight and high-performance components for a range of applications such as aircraft engines, turbines, and structural parts [4]. The aerospace industry has long been focused on reducing the weight of aircraft components to improve fuel efficiency and reduce emissions. PBF-LB provides a unique opportunity to achieve this goal by allowing for the creation of complex geometries with optimized internal structures, reducing material waste and enabling the production of lightweight components with high strength-to-weight ratios [1, 3, 5]. Moreover, PBF-LB enables the creation of parts with specific microstructures, such as controlled porosity or grain size distribution, which can improve their mechanical properties and performance. The aerospace industry has already seen promising results from PBF-LB applications, such as the production of fuel nozzles and complex heat exchangers for aircraft engines [6, 7]. However, to fully exploit the potential of PBF-LB in aerospace applications, a deeper understanding of the microstructural features and their impact on mechanical properties is needed and standardized guidelines and methods for quality assurance and verification need to be developed [8]. The study presented here aims to contribute to this understanding by utilizing a multimodal and multiscale correlative microscopy approach to investigate the microstructure of AlSi10Mg components made by PBF-LB, which finds applications in numerous fields of industries such as the automobile and aerospace sectors [9], including optical microscopy (OM), scanning electron microscopy (SEM), energy dispersive X-ray spectroscopy (EDS), electron backscatter diffraction (EBSD) and X-ray microscopy (XRM). Correlative microscopy refers to the integration of different investigations modalities to provide a comprehensive understanding of a sample's structural and functional properties. XRM is a valuable tool in materials characterization that can provide information on the microstructure and composition of an object non-destructively by exploiting radiation matter interaction. XRM has been involved in a wide range of applications such as aerospace [10, 11], energy materials research [12–14], electronics and semiconductors [15, 16], cultural heritage [17–20], biomedical engineering [21, 22], and life sciences [23]. XRM is a powerful technique that enables a wide range of 2D/3D experiments across multiple length scales. OM on the other hand, provides detailed information about the surface properties of the sample, such as morphology and topography. SEM is a powerful technique for high-resolution imaging of the surface of samples at a nanoscale level. Additionally, when coupled with EDS, SEM provides chemical information about the sample composition. These characterization techniques are often employed separately and are rarely compared to each other. Our study presents a multiscale, multimodal, comprehensive, and systematic analysis of the microstructure of the AlSi10Mg alloy using a combination of correlative microscopy techniques. The innovation of the proposed work lies in thoroughly comparing and discussing different methods. It involves a detailed exploration of each method, highlighting their unique characteristics, providing evidence of their positive aspects, and acknowledging the limitations of other methods. The integration of these techniques offers a unique advantage in the analysis of complex systems and structures. By optimizing the performance of PBF-LB fabricated components, the aerospace industry can improve the safety, efficiency, and sustainability of aircraft, while also reducing costs and production times.

2 Materials and methods

2.1 Sample fabrication

AlSi10Mg samples were fabricated by the company BEAMIT (Fornovo di Taro (PR) 43045 Italy) [24] in a production plant model SLM280HL Twin. Detailed information about the powder can be found in Table 1, while the process parameters and the build chamber atmosphere are reported in Table 2. The analysis described in the following was carried out on vertical as-built cylindrical specimens whose dimensions are 8 mm (diameter) × 36 mm (height).

2.2 Density measurement

Sample density was determined in accordance with the ASTM D792-20 standard, with a reference value of 2.68 g/cm^3 considered as 100%.

Table 1 Key characteristics of AlSi10Mg metal powder for PBF-LB fabrication: tap density, flow rate, and particle size distribution, aligned with company purchase specifications, as provided by the powder supplier

Powder information—chemical composition wt%			
Element	Results wt%	Element	Results wt%
Al	bal	Pb	0.001
Si	10	Sn	< 0.001
Fe	0.12	Ti	0.04
Cu	0.001	C	< 0.005
Mn	0.005	H	0.002
Mg	0.31	N	< 0.002
Ni	0.004	O	0.028
Zn	0.002	other	< 0.02
Particle size distribution by Laser Diffraction (Microtrac) ASTM-B822/B821 Internal method			
Vol %	D10	D50	D90
Results	30 μm	44 μm	63 μm
Tap density ASTM-B527 Internal method		g/cm^3	1.8
App. density Air@ 30%RH, 23°C ASTM-B417 Internal method		g/cm^3	1.52

Table 2 Process parameters and build chamber atmosphere specifications

Process parameters	
Layer thickness	50 μm
Laser power	350 W
Scan speed	1150 mm/s
Hatch distance	170 μm
Plate temperature	150 °C
Build chamber atmosphere	
Equipment	SLM280HL
Build volume	280280 * 365 mm
Atmosphere	Argon

2.3 Sample preparation

Two metallographic samples were prepared for each test piece, with one section being perpendicular and the other parallel to the cylinder's direction of construction (z-axis). All sections obtained from the coupons and test pieces were embedded in *Multifast black* phenolic resin (Struers), and polished using 1 mm diamond paste (DP-Suspension, Struers). The microstructure of the aluminum alloy was revealed using an etching solution containing Keller's reagent (2.5%v/v HNO_3, 1.5%v/v HCl, 1%v/v HF, 95%v/v H_2O).

2.4 Optical microscopy (OM)

OM examination was carried out using a Leica M205C and Leica DM6000M optical microscopes and a Hirox KH-7700 digital microscope.

2.5 Scanning electron microscopy (SEM)

SEM investigation was conducted using a field emission gun scanning electron microscope (FE-SEM) (Ultra-Plus, Carl Zeiss, Oberkochen, Germany) equipped with an Energy Dispersive X-ray Spectroscopy (EDS) detector (INCA X-EDS Oxford Instruments United Kingdom) and an Electron Backscattered Diffraction (EBSD) detector (C Nano Oxford Instruments United Kingdom), using a 0.5 µm scanning step size. FE-SEM analysis samples cleanup was carried out in ultrasonic bath with Methyl Acetate for 20 min at 40° C. Methyl Acetate (98%) was purchased from Sigma Aldrich.

2.6 X-ray microscopy (XRM)

XRM scans were performed using a ZEISS Xradia Versa 610 available at the Research Center on Nanotechnology Applied to Engineering of Sapienza (CNIS) that is part of the open Infrastructure for "Advanced Tomography and Microscopies (ATOM)" of Sapienza University of Rome. The first low resolution scan was conducted to obtain an overall understanding of the porosity throughout the structure. Subsequently, the Scout-and-Zoom approach was employed to obtain three additional scans, each with a smaller pixel size, to study the porosity at different length scales.

Low-Resolution Scan - Entire sample (pixel size 19.31 µm): Objective 0.4x, FOV (34,606.25 × 19,775) µm, Bin 2, Exposure time 1 s, Source Filter LE6, Voltage 80 kV, Power 10 W, number of projections 1601. The sample was scanned using the vertical stitch mode available in the Scout-and-Scan Control System (V. 16.1.14271.44713).

High-Resolution Scan – Volume of Interest 1 (pixel size 16.82 µm): Objective 0.4 ×, FOV (17,226 × 17,226) µm, Bin 2, Exposure time 1 s, Source Filter LE6, Voltage 80 kV, Power 10 W, number of projections 1601.

High-Resolution Scan – Volume of Interest 2 (pixel size 3.62 µm): Objective 4 ×, FOV (3669.6 × 3668.6) µm, Bin 2, Exposure time 2 s, Source Filter LE6, Voltage 80 kV, Power 10 W, number of projections 2401.

High-Resolution Scan – Volume of Interest 3 (pixel size 1.51 µm): Objective 4 ×, FOV (1525.1 × 1525.1) µm, Bin 2, Exposure time 12 s, Source Filter LE6, Voltage 80 kV, Power 10 W, number of projections 3001.

2.7 Reconstruction of XRM datasets

Using the Scout-and-Scan Control System Reconstructor (V. 16.1.14271.44713) XRM datasets were reconstructed employing the Feldkamp-Davis-Kress (FDK) algorithm.

2.8 Image analysis and processing

Once the XRM datasets were reconstructed, Dragonfly Pro (Version 2022.1) from Object Research Systems [25] was employed to filter and process the images.

3 Results and discussion

3.1 Optical and scanning electron microscopy analysis

A CAD representation of the AlSi10Mg sample fabricated via PBF-LB with a density of 99.4 ± 0.1% is reported in Fig. 1a. The cut plane orthogonal to the construction axis (red) and the parallel one (blue) are highlighted. A metallography obtained from the orthogonal section (red) with respect to the construction axis is shown in Fig. 1b. The traces (hatch) left by the laser scan can be distinguished as they are oriented along bundles of parallel lines, but with different angles between layers. The traces are parallel in a single layer and rotated, typically at an angle of 67°, when passing to the next layer to maximize the number of orientations, thus mitigating the anisotropy problems of these materials [26]. The width of the trace corresponds to the width of the melt pool, as will be extensively discussed later. The average width of the traces is 170 ± 30 microns, based on a minimum of 10 measurements. The entire surface of the specimen appears to be free of obvious defects, with sporadic almost spherical black areas, associated with holes generated when a vapor-filled cavity is formed by the laser beam, generally referred to as keyhole in literature [27, 28].

Fig. 1 **a** CAD representation of the sample AlSi10Mg fabricated via PBF-LB with a density of 99.4 ± 0.1%. The cut plane orthogonal to the construction axis (red) and the parallel one (blue) are reported. **b** A metallography obtained from the orthogonal section is depicted. The traces (hatch) left by the laser scan, with an average width of 170 ± 30 μm, can be distinguished revealing a rotation of 67° between layers and pores (keyholes) are highlighted by yellow circles. **c** The specimen is characterized by the presence of irregularly shaped particles which can be associated with the existence of oxides according to their geometry and size. **d** Enlarged view of a keyhole obtained using a digital microscope revealing a height of 15.22 μm and a width of 28.72 μm. **e** The edge of the specimen is significantly different from the core, being composed of overlapping coincident traces, no longer phased by 67°

Enlarged view of a keyhole
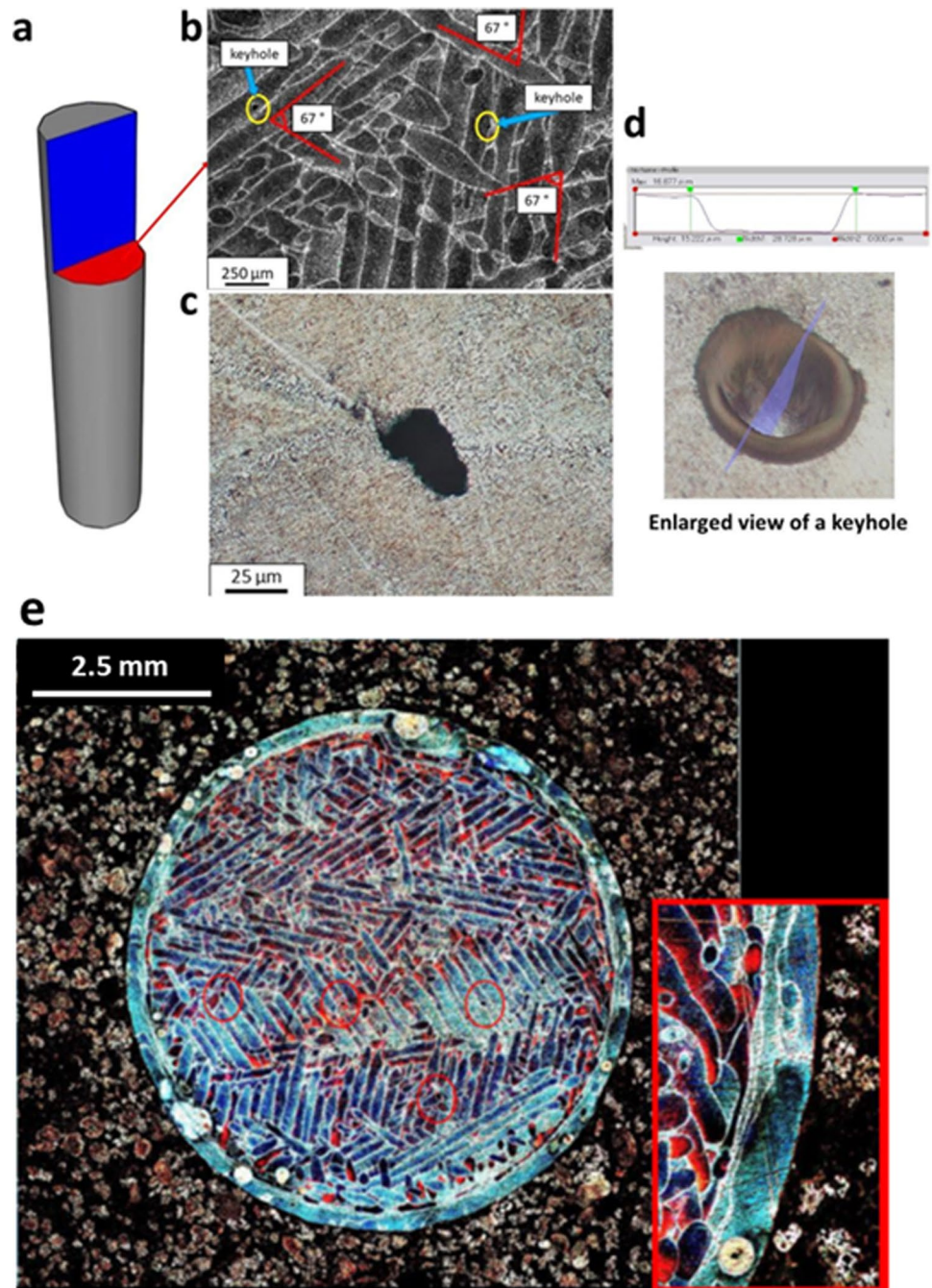
Another type of defect found on all specimens consists of irregularly shaped particles, as shown in Fig. 1c compatible in shape and size with the presence of oxides, as reported in the literature [29].

An enlarged view of a keyhole obtained using a digital microscope revealing a height of 15.22 μm and a width of 28.72 μm is depicted in Fig. 1d. Observing Fig. 1e, it is evident how the edge of the specimen is significantly different from the core, being composed of overlapping coincident traces, no longer phased by 67°. The presence of non-continuous traces in the upper layers, as observed in Fig. 1b, depends on the imperfect perpendicularity between the construction axis of the specimen and the sectioning plane, as well as on variations in the depth of the trace during the fabrication process. The situation is depicted in Fig. 2 where a depth variation of the laser scan is reported for the purpose of visualization. Note that the depth variation in Fig. 2 is stressed and out of the scale, hence should be considered just as an explanation of the phenomenon. A close-up of a region where scanning traces intersect is shown in Fig. 3, with the

Fig. 2 The presence of non-continuous traces depends on the imperfect perpendicularity between the construction axis of the specimen and the sectioning plane, as well as on variations in the depth of the trace during the manufacturing process. The depth variation reported in this figure is stressed and out of the scale, hence should be considered just for the purpose of visualization
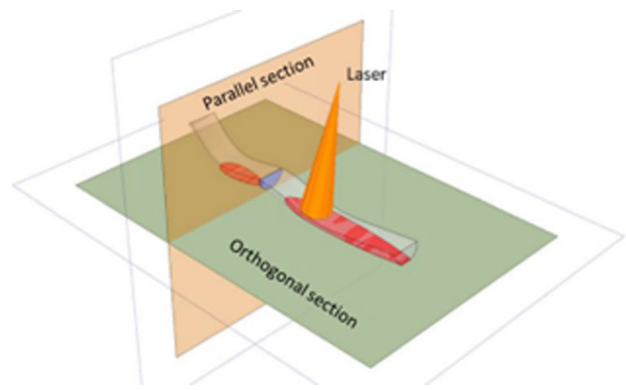
intersections highlighted in red dotted lines. It is evident that the edge of the single scan is not continuous, but rather composed of a cellular structure, as clarified in the following SEM investigation.

The average hardness value of the samples, obtained using the Micro Vickers method (ASTM E384), is 140 ± 5 HV. The applied load was 30 N, and the reported result is the average of at least 50 measurements. This value is significantly higher than that of the same alloy obtained by casting in the annealed state, which ranges from 95 to 105 HV [29]. The typical microstructure of the AlSi10Mg alloy obtained by PBF-LB is shown in Fig. 4a: a solid solution of aluminum-alpha (Al-α), depicted in black, surrounded by a continuous network of Al-Si eutectic, represented in white. The elemental composition of the eutectic, obtained through EDS, is reported in Fig. 4b. The silicon content is slightly above the nominal 10% revealing that the faster cooling results in a supersaturated pseudo-eutectic microstructure [28]. The microstructure observed Fig. 4a is consistent with the *cellular structure*, as defined in the literature [30]. A schematization of the PBF-LB fabrication process is represented in Fig. 5a. At the center of the scan trace, the material undergoes a cooling process to the ambient temperature, resulting in the formation of a fine cellular structure. The production process of the component involves slightly overlapping each scanning trace with the previously deposited one to maximize fusion. This technique results in a portion of the already deposited material experiencing a second temperature increase like that occurring during welding. This process initially leads to the coarsening of the structure, followed by the formation of a heat affected zone (HAZ). The HAZ is characterized by the disruption of the continuous eutectic network, resulting in the formation of a disordered structure, as shown in Fig. 5b [31]. The region observed using SEM is reported at lower magnification in the OM image, in Fig. 5b.

The visible traces observed via optical microscopy in the section parallel to the construction axis, highlighted in blue in Fig. 1a and reported in Fig. 6, also show a change in microstructure, with a transition from fine to coarse cellular structure and the presence of a thermally altered overlapping zone. In the micrograph of Fig. 6, the directionality of heat transfer is noticeable: the cellular microstructure in the fusion pools is not equiaxed but presents an elongation towards the border of the pool, which is the direction of maximum heat removal.

A Building Direction (Z0) Inverse Pole Figure (IPF) map obtained via EBSD is presented in Fig. 7. The image proves the smaller size of the grains in the pool border compared to the center. This observation is consistent with the previous statements. Despite the increase in size of the matrix in the cellular structure towards the melting pool border, the grain size decreases, as illustrated in Fig. 7. It is noteworthy that nearly all grains exhibit an equiaxed shape, as anticipated for a section perpendicular to the building direction, where isotropic heat diffusion occurs in this plane.

Fig. 3 Red dotted lines highlight a region where scanning traces intersect. It is evident that going from the center to edge of the scan trace the matrix of the cellular structure increases in size
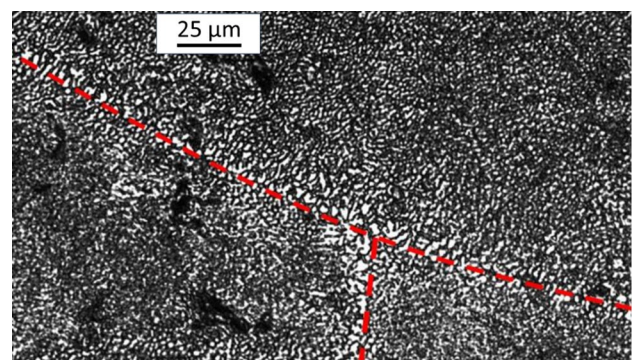
Fig. 4 **a** The typical micro-structure of the AlSi10Mg alloy obtained by PBF-LB is composed of a solid solution of aluminum-alpha supersaturated in Si (in black) surrounded by a continuous network of Al-Si eutectic (in white). **b** Elemental composition of the Al-Si eutectic, obtained through EDS
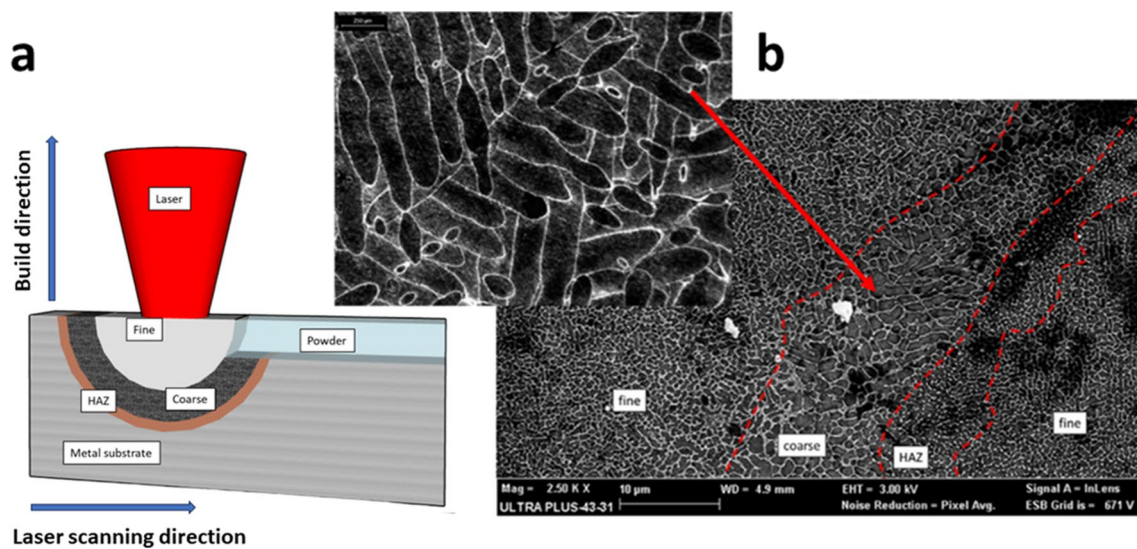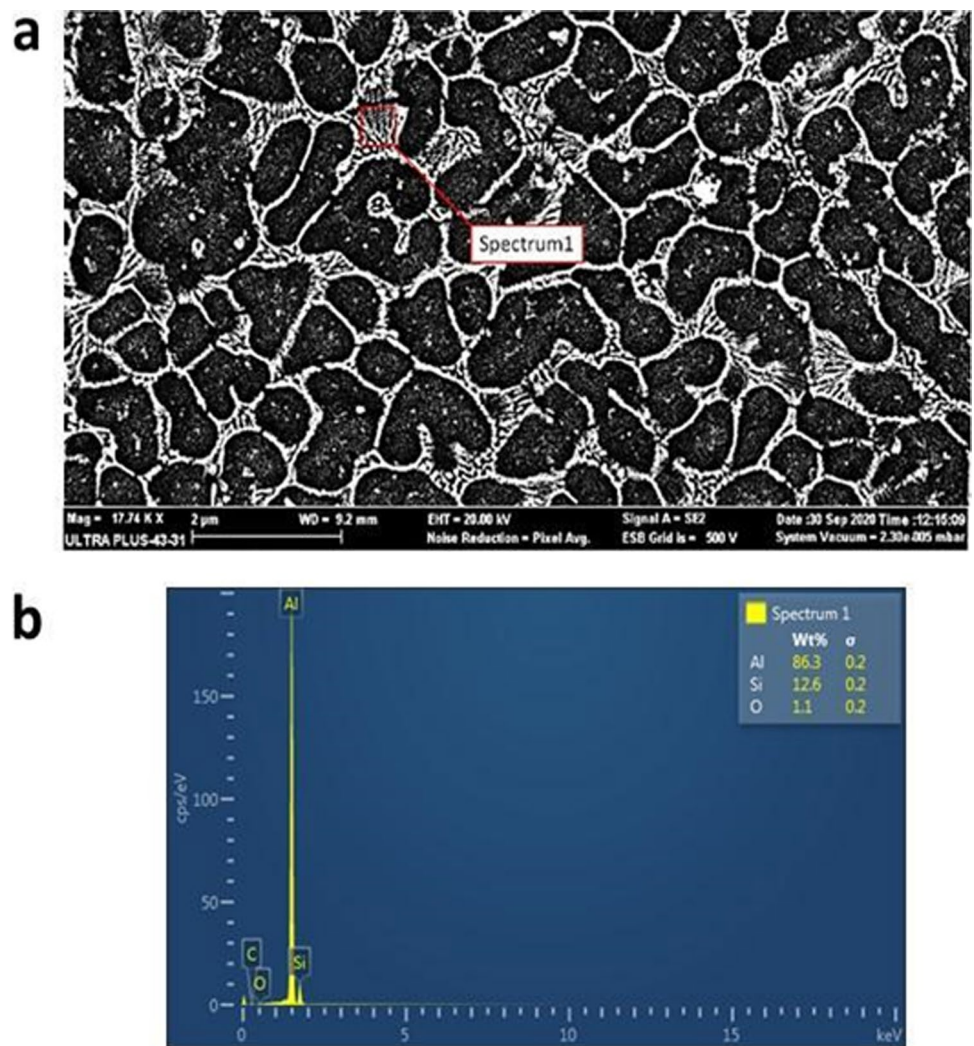

Fig. 5 **a** Schematization of the PBF-LB fabrication process. **b** SEM micrograph showing fine, coarse and HAZ regions. The region observed using SEM, is reported at lower magnification in the OM image [31]

Fig. 6 The micrograph related to the section parallel to construction axis revealed a change in the microstructure, with a transition from fine to coarse cellular structure and a thermally altered zone. This micrograph highlights the directionality of heat transfer: the cellular structure in the fusion pools is not equiaxed but shows an orientation towards the border of the pool, which is the direction of maximum heat removal
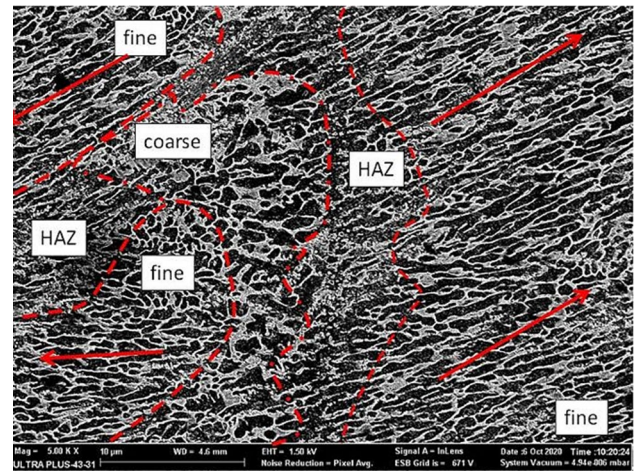
Fig. 7 Inverse pole figure (IPF) map in the building direction (Z0), normal to the plane of the image. It is worth noting that the grains at the border of the pool exhibit a smaller size compared to those in the center
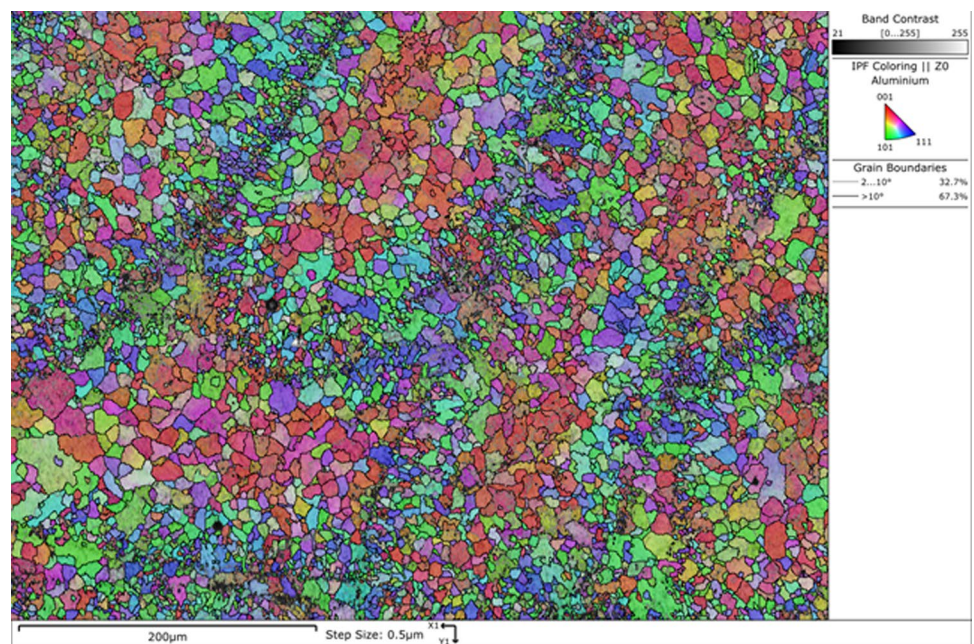
However, the exception is observed in the smaller grain present in the border which exhibits an elongated shape. This elongated shape confirms the occurrence of strong heat diffusion through the border of the melting pool [32].

Upon observing the EDS map of the same area, as presented in Fig. 8, it is evident that the defects in the Al-Si matrix (depicted by the black areas in the Al and Si maps) are primarily composed of O, C, and Fe. This confirms the presence of oxide defects, as discussed earlier. Furthermore, the Si map illustrates the scan tracks distinctly. Si has a noticeable difference in melting temperature compared to Al, and this gradient is the cause of the slight variation in Si distribution among the samples. This is due to the segregation mechanism, a well-known effect in literature [33].

Two subsets of the IPF map from Fig. 7 are reported in Fig. 9 where grain sizes smaller and larger than 7 μm are considered separately. The reason for this subdivision is that a preferential orientation of the grains is observed, and 7 μm is found to be the optimal value that highlights this feature. It should be noticed that 2 μm is the smallest size that can be resolved with the current resolution, where the step size is 0.5 μm. The smaller grains (2 μm < Ø < 7 μm) demonstrate a 101 preferred orientation in the build direction, whereas the coarser grains (Ø > 7 μm) show a 001 preferred orientation. No preferred orientations are observed in the x and y directions.
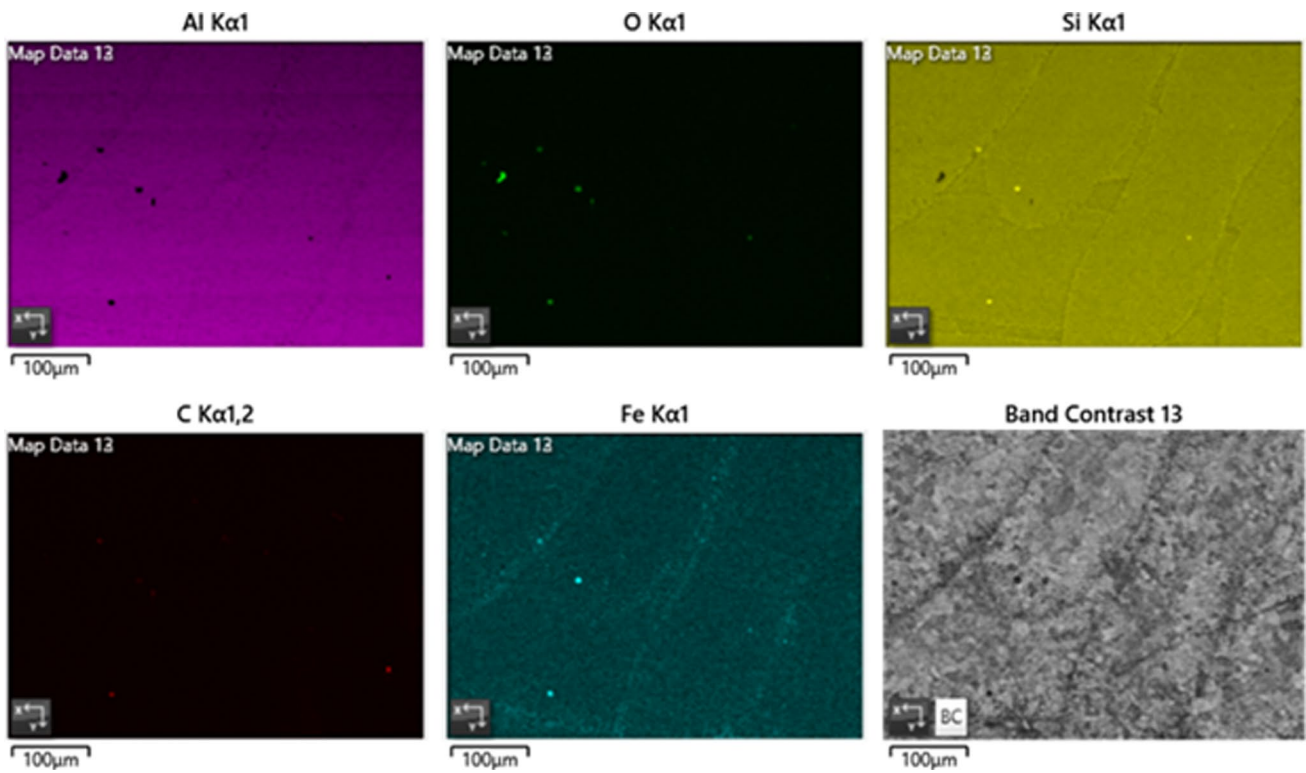
Fig. 8 Energy dispersive X-ray spectroscopy (EDS) map of the same area shown in Fig. 7
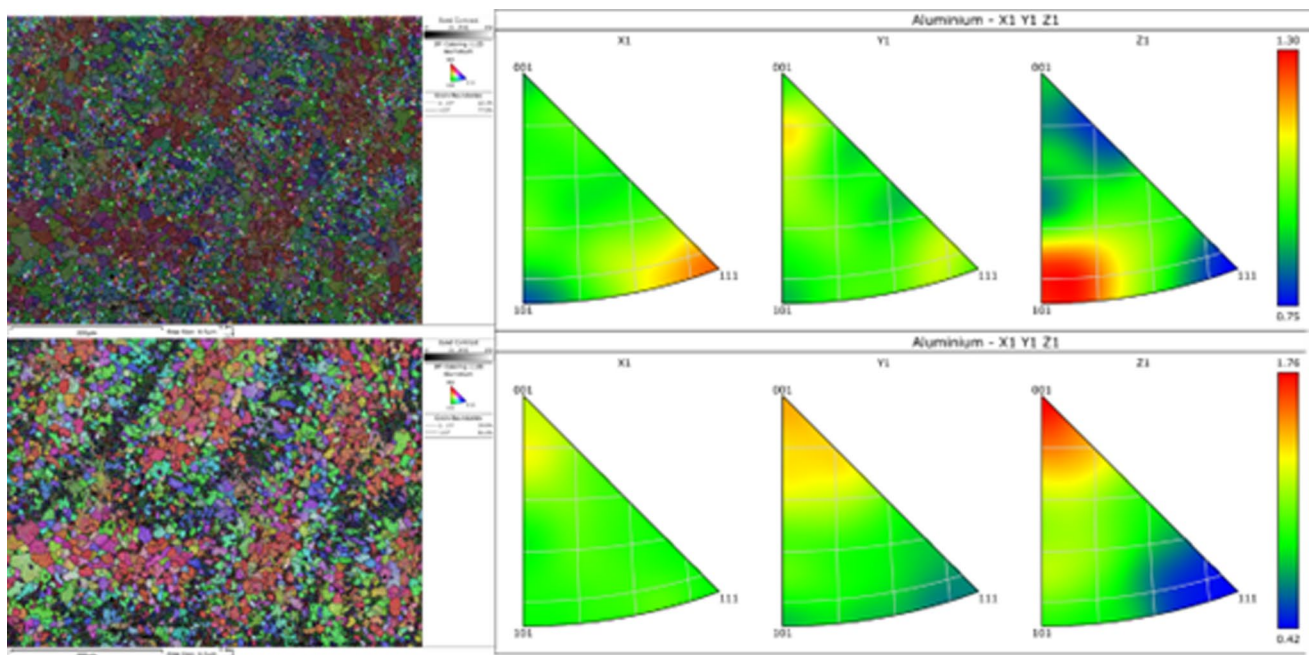

Fig. 9 The preferred crystallographic orientation exhibited by small grains (2 µm < Ø < 7 µm) in the building direction is 101, while coarser grains (Ø > 7 µm) show a preferred orientation of 001. No preferred orientation is observed in the x and y directions

3.2 X-ray microscopy analysis

Multiscale XRM was employed to investigate the specimen with specific regard to keyhole size distribution at different length scales. XRM is the most suitable tool for this purpose since it allows non-destructive three-dimensional investigation revealing internal and hidden features of the specimen with minimum sample preparation [34–36]. A first low-resolution scan (pixel size 19.31 µm) was performed to get a general representation of the AlSi10Mg component obtained via PBF-LB. In this case, the vertical stitch mode was employed to investigate the entire sample without compromising the resolution. The 3D reconstruction of the sample is reported in Fig. 10a (left) as well as 2D slices acquired along the XZ (red), ZY (green), and XY (blue) planes (right). An enlarged view of a selected region of the slice in the ZY plane is reported and highlighted by the yellow box in Fig. 10b. Several keyhole diameters ranging from 47 to 75 µm are annotated. It should be noticed that some keyholes are characterized by smaller diameter, however the resolution is not suitable for their characterization. For this purpose, we adopted a multiscale approach to get a better understanding of porosity distribution over the sample with higher resolution. Three volumes of interest (VOIs) were identified to perform high-resolution XRM. The so-called Scout-and-Zoom procedure was adopted using Dragonfly Pro (V. 2022.1) from Object Research Systems (ORS) [25] to precisely center the VOI along the reference axis during the scan. The first volume of interest, named VOI 1, was investigated using a pixel size 16.82 µm and is delimited by the red cylinder in Fig. 11 (left).

The region of interest (ROI) containing the pore space was segmented using a histogram-based thresholding method and its three-dimensional representation is shown in Fig. 11 (right). The same method was used for pore analysis in the other two VOIs. A second high-resolution scan (pixel size 3.62 µm) was performed on a selected volume
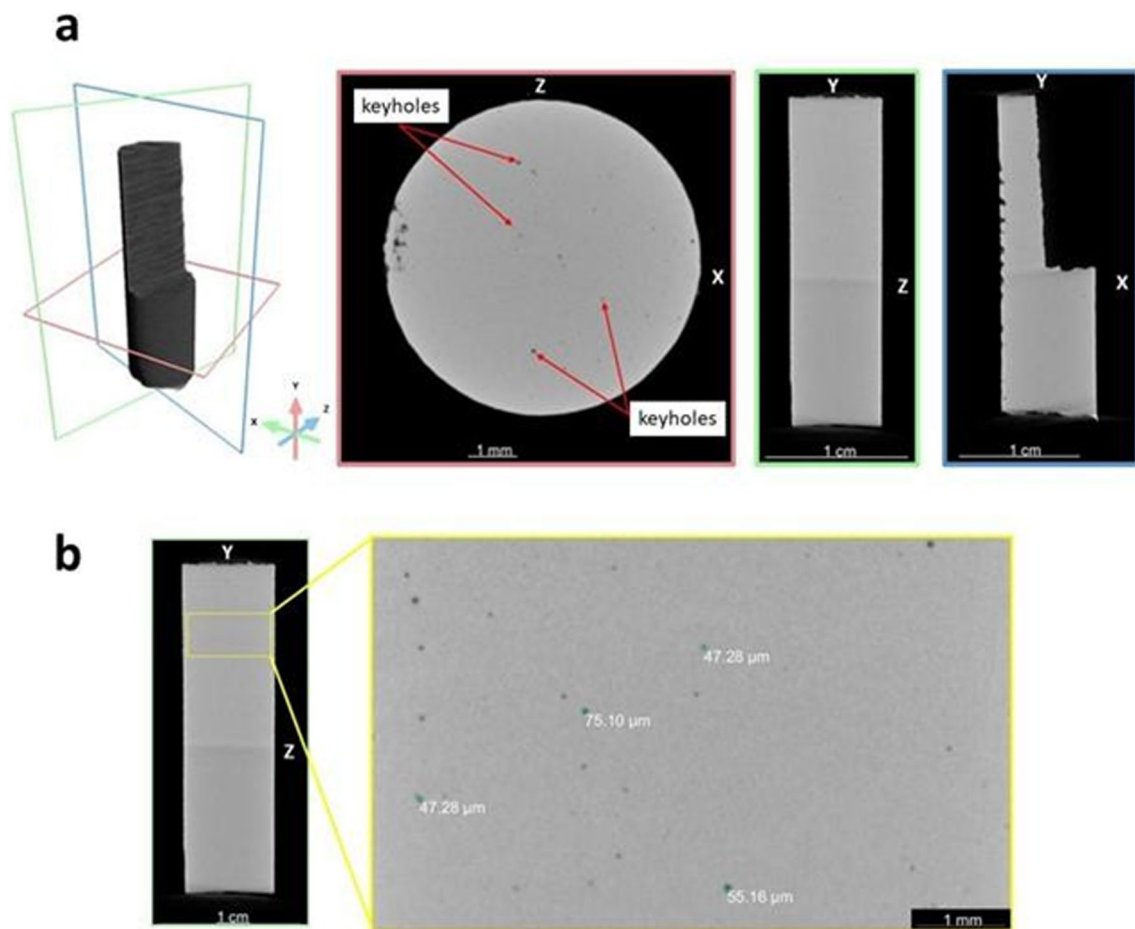

Fig. 10 **a** 3D reconstruction of the AlSi10Mg component obtained via PBF-LB (left) and 2D slices acquired along the XZ (red), ZY (green) and XY (blue) planes (right). **b** The enlarged view of the region highlighted by the yellow box was used to point out several keyholes with a diameter ranging from 47 to 75 µm. A multiscale XRM approach is required to get a deeper understanding of porosity behavior over the sample
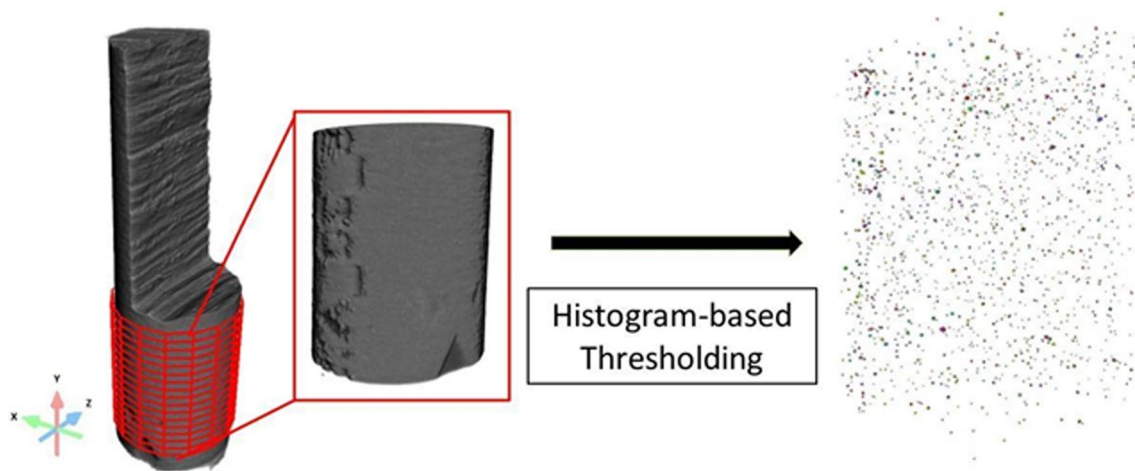
Fig. 11 The selected VOI is delimited by the red cylinder (left). The region of interest (ROI) containing the pore space was segmented using a histogram-based thresholding (right)

of interest, called VOI 2. The pore spaces from VOI 1 and VOI 2 were transformed into a multi-ROI to perform an object analysis and extract the pores mean Feret diameter. The Feret diameter is measured by selecting the two points on opposite sides of the object's boundary that are farthest apart and measuring the distance between them in various directions. The mean Feret diameter is then calculated as the average of all these measurements. Therefore, this parameter is particularly suitable in applications such as pore size analysis.

A comparison between results obtained for VOI 1 and VOI 2 is reported in Fig. 12 as well as the blue cylinder that highlights the internal volume of the sample that we called VOI 2. Observing the mean Feret diameter distribution histograms reported in Fig. 12a-b referred to VOI 1 and VOI 2 a significant variation in the mean value from 74.52 μm to 23.65 μm emerges. These results suggest further XRM experiments to reach a higher resolution and investigate the pores behavior with finer detail. Hence, a third volume of interest, VOI 3, was selected to be scanned using a pixel size of 1.51 μm. The same analytical approach was used for segmentation and object analysis. In this case, the mean value of the mean Feret diameter distribution referred to VOI 3 is 10.60 μm, as shown in Fig. 13. This behavior can be explained as follows. When using XRM to analyze the porosity of a material, the size of the pixels used in the scan can have a significant effect on the measured pore size. When using a larger pixel size of 16.82 μm, the image of the sample would contain fewer pixels and each pixel would represent a larger area of the sample. As a result, small pores would be smoothed out and merged with neighboring pores, leading to an overestimation of the pore size. On the other hand, large pores would be more accurately represented, and their size would be less influenced by pixel size [37]. This could explain the larger mean value of the mean Feret diameter of pores observed with a larger pixel size. When using a smaller pixel size of 3.62 μm or 1.51 μm, the XRM image would contain more pixels and each pixel would represent a smaller area of the sample. This would enable the detection of smaller pores, which would lead to a more accurate measurement of pore size, especially for small pores. As a result, the measured mean value of the mean Feret diameter of pores would decrease as the pixel size decreased.

In summary, the variation of the mean value of the mean Feret diameter of pores with changing pixel size in X-ray microscopy scans is due larger pixel sizes tend to overestimate pore size while smaller pixel sizes tend to provide a more accurate measurement of pore size, especially for small pores.

XRM results highlight the presence of a matrix of pores that evolves at different length scales which can significantly affect the mechanical properties of the sample. Porosity can reduce the strength, stiffness, and ductility of the material, as well as increase its susceptibility to fatigue and fracture [38–43]. The larger the pore size, the more significant the reduction in strength and stiffness [41, 44]. However, small pores can also play a role in reducing strength and stiffness by acting as stress concentration points [45]. The pore matrix dataset can be used to inform different damage models as in [46, 47] and implemented in a set of global finite element simulations. By simulating the mechanical behavior of a representative volume element of the material, the effect of the evolving matrix of pores on the mechanical properties of the material can be investigated. The simulation results can be used to optimize the properties of materials for specific applications by understanding how porosity affects the mechanical behavior of the material.
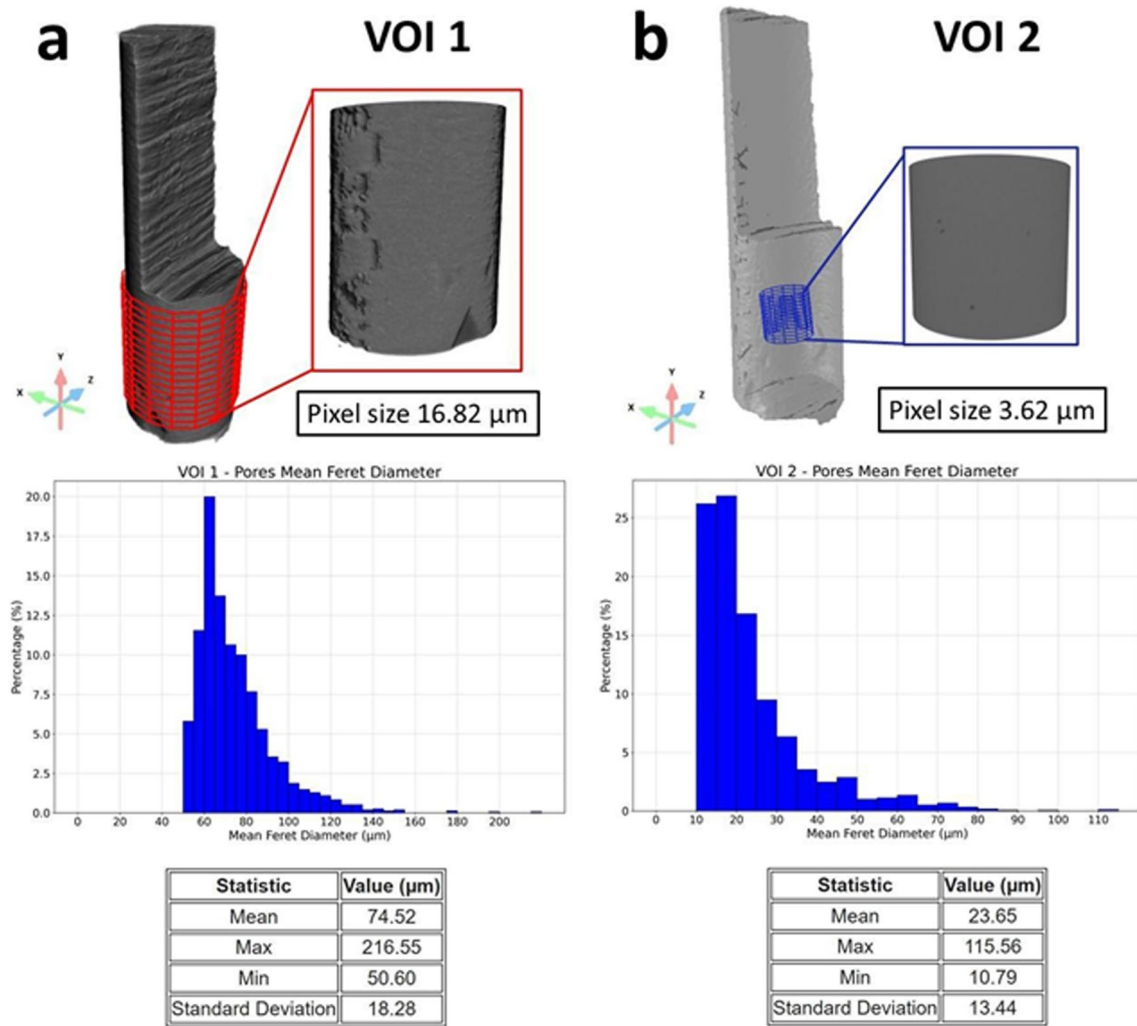
Fig. 12 Comparison between mean Feret diameter distributions related to the pores from (**a**) VOI 1, delimited by the red cylinder (pixel size 16.82 μm), and (**b**) VOI 2 highlighted by the blue cylinder (pixel size 3.62 μm). A significant variation in the mean value from 74.52 μm (VOI 1) to 23.65 μm (VOI 2) emerges. This suggests performing further experiments to reach higher resolutions

4 Conclusions

In this study, a multimodal and multiscale correlative microscopy approach was employed to investigate the microstructure of AlSi10Mg components fabricated by Powder Bed Fusion—Laser Beam (PBF-LB), a promising additive manufacturing technique for the aerospace industry. The study aimed to provide a comprehensive understanding of the relationship between the fabrication process and the effective microstructure of the components involving a detailed exploration of each investigation method, highlighting their unique characteristics, providing evidence of their positive aspects, and acknowledging the limitations of other methods. Optical Microscopy (OM) was used to investigate the traces (hatch) left by the laser scan revealing that they are oriented along bundles of parallel lines, with a rotation angle of 67° between layers to mitigate anisotropy issues. The average width of the traces was measured to be 170 ± 30 microns. The presence of irregularly shaped particles, likely oxides, was also observed. Scanning Electron Microscopy (SEM), coupled with Energy Dispersive X-ray Spectroscopy (EDS), was used to characterize the chemical composition and microstructure of AlSi10Mg alloy highlighting the transition of the matrix of the cellular structure from fine to coarse zones and the presence of a Heat Affected Zone (HAZ). Electron Backscatter Diffraction (EBSD) showed that the grains at the border of the pool exhibit a smaller size compared to those in the center. EBSD revealed a preferred crystallographic orientation for small (101) and large (001) grains. Then, multiscale X-ray
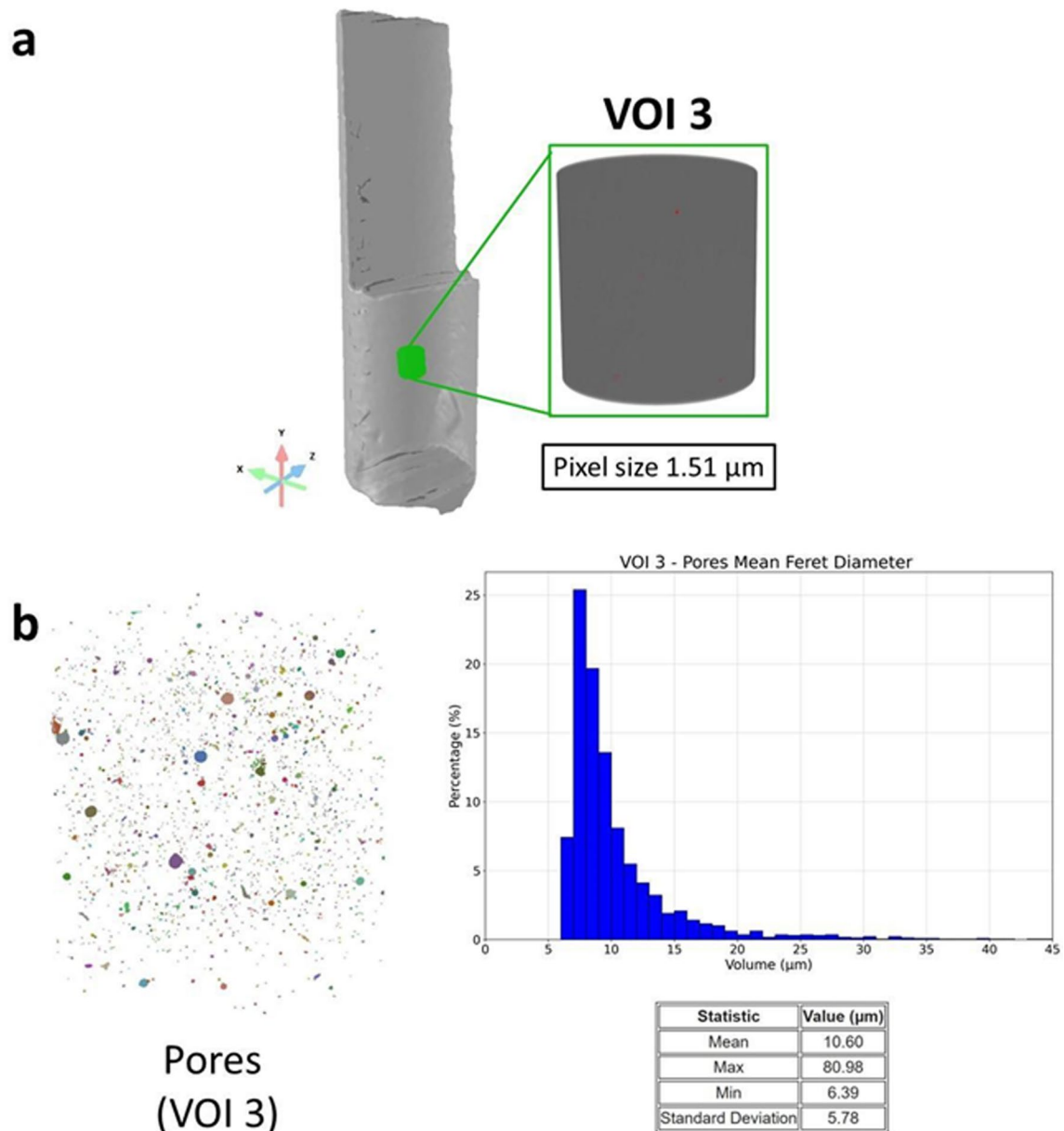
Statistic	Value (µm)
Mean	10.60
Max	80.98
Min	6.39
Standard Deviation	5.78

Fig. 13 **a** The third volume of interest, named VOI 3, scanned with a pixel size of 1.51 µm is defined by the green cylinder. **b** The pore space of VOI 3 was added to a multi-ROI to perform object analysis and extract the mean Feret diameter distribution. This step revealed a mean value of 10.60 µm. The variation of the mean value of the mean Feret diameter of pores with changing pixel size in X-ray microscopy scans is due to the fact that larger pixel sizes tend to overestimate pore size while smaller pixel sizes tend to provide a more accurate measurement of pore size, especially for small pores

Microscopy (XRM) was employed to investigate the pore (*keyholes*) size distribution. XRM results highlight the presence of a pores matrix that evolves at different length scales. Further studies will involve the use of the pore matrix dataset to inform different damage models and its implementation in a set of global finite element simulations. By simulating the mechanical behavior of a representative volume element of the material, the effect of the evolving matrix of pores on the mechanical properties of the material can be investigated. The simulation results, coupled with our multimodal and multiscale correlative microscopy approach, can be used to optimize the properties of materials for specific applications by understanding how porosity affects the mechanical behavior of the material.

Data and code availability The data that support the findings of this study are available from the corresponding author F.C upon request.

Declarations

Ethics approval and consent to participate Not applicable.

Competing interests The authors have no conflicts of interest to declare. All co-authors have seen and agree with the contents of the manuscript and there is no financial interest to report.

References

1. Zhai Y, Lados DA, LaGoy JL. Additive manufacturing: making imagination the major limitation. J Miner Metals Mater Society (TMS). 2014;66:808–16.
2. DebRoy T, Wei H, Zuback J, Mukherjee T, Elmer J, Milewski J, Beese A, Wilson-Heid A, De A, Zhang W. Additive manufacturing of metallic components—process, structure and properties. Prog Mater Sci. 2018;92:112–224.
3. Yap CY, Chua CK, Dong ZL, Liu ZH, Zhang DQ, Loh LE, Sing SL. Review of selective laser melting: materials and applications. Appl Phys Rev. 2015; 2(4).
4. Seabra M, Azevedo J, Araújo A, Reis L, Pinto E, Alves N, Santos R, Mortágua JP. Selective laser melting (SLM) and topology optimization for lighter aerospace componentes. Proc Struct Integr. 2016;1:289–96.
5. Haase C, Bültmann J, Hof J, Ziegler S, Bremen S, Hinke C, Schwedt A, Prahl U, Bleck W. Exploiting process-related advantages of selective laser melting for the production of high-manganese steel. Materials. 2017;10(1):56.
6. Sotov AV, Agapovichev AV, Smelov VG, Kokareva VV, Dmitrieva MO, Melnikov AA, Golanov SP, Anurov YM. Investigation of the IN-738 superalloy microstructure and mechanical properties for the manufacturing of gas turbine engine nozzle guide vane by selective laser melting. Int J Adv Manuf Technol. 2020;107:2525–35.
7. Chiumenti M, Neiva E, Salsi E, Cervera M, Badia S, Moya J, Chen Z, Lee C, Davies C. Numerical modelling and experimental validation in selective laser melting. Addit Manuf. 2017;18:171–85.
8. National Institute of Standards and Technology, "Measurements Science Roadmap for Metal-Based Additive Manufacturing," 2013. [Online]. Available: https://www.nist.gov.
9. Martin JH, Yahata BD, Hundley JM, Mayer JA, Schaedler TA, Pollock TM. 3D printing of high-strength aluminium alloys. Nature. 2017;549:365–9.
10. du Plessis A, Rossouw P. X-ray computed tomography of a titanium aerospace investment casting. Case Stud Nondestruct Testing Eval. 2015;3:21–6.
11. Chowdhury P, Sehitoglu H, Rateick R. Damage tolerance of carbon–carbon composites in aerospace application. Carbon. 2018;126:382–93.
12. Cognigni F, Pasquali M, Prosini PP, Paoletti C, Aurora A, Scaramuzzo FA, Rossi M. X-Ray microscopy: a non-destructive multi-scale imaging to study the inner workings of batteries. ChemElectroChem. 2023;10(70):e202201081.
13. Dini D, Cognigni F, Passeri D, Scaramuzzo AF, Pasquali M, Rossi M. Review—multiscale characterization of li-ion batteries through the combined use of atomic force microscopy and X-ray microscopy and considerations for a correlative analysis of the reviewed data. J Electrochem Soc. 2021;168(12):126522.
14. Trogadas P, Taiwo OO, Tjaden B, Neville TP, Yun S, Parrondo J, Ramani V, Coppens M-O, Brett DJL, Shearing PR. X-ray micro-tomography as a diagnostic tool for the electrode degradation in vanadium redox flow batteries. Electrochem Commun. 2014;48:155–9.
15. Hartfield C, Schmidt C, Gu A, Kelly ST. From PCB to BEOL: 3D X-ray microscopy for advanced semiconductor packaging. In: IEEE International Symposium on the Physical and Failure Analysis of Integrated Circuits (IPFA), Singapore, 2018.

16. Zulkifli SM, Zee B, Qiu W, Gu A. High-res 3D X-ray microscopy for non-destructive failure analysis of chip-to-chip micro-bump interconnects in stacked die packages, In: IEEE 24th International Symposium on the Physical and Failure Analysis of Integrated Circuits (IPFA), Chengdu, 2017.

17. Bernabale M, Cognigni F, Mura F, Nigro L, Montanari D, Rossi M, De Vito C. 3D imaging of micro-segregation and corrosion behavior of alloying elements in archaelogical artefacts from Motya (Sicily, Italy). Corros Sci. 2023;211:110900.

18. Bernabale M, Cognigni F, Nigro L, Rossi M, De Caro T, De Vito C. A comprehensive strategy for exploring corrosion in iron-based artefacts through advanced Multiscale X-ray Microscopy. Sci Reports. 2022;12(1):6125.

19. Bernabale M, Cognigni F, Nigro L, Rossi M, De Vito C, Conventional and advanced techniques for archaelogical diagnostic of iron artefacts. In: 2022 IMEKO TC-4 International COnference on Metrology for Archaeology and Cultural Heritage University of Calabria, Cosenza, 2022.

20. Gonzalez V, Cotte M, Vanmeert F, de Nolf W, Janssens K. X-ray diffraction mapping for cultural heritage science: a review of experimental configurations and applications. Chem Eur J. 2019;26(8):1703–19.

21. Razavi M, Qiao Y, Thakor AS. Three-dimensional cryogels for biomedical applications. J Biomed Mater Res Part A. 2019;107(12):2736–55.

22. Bachtiar EO, Erol O, Millrod M, Tao R, Gracias DH, Romer LH, Kang SH. 3D printing and characterization of a soft and biostable elastomer with high flexibility and strength for biomedical applications. J Mech Behav Biomed Mater. 2020;104:103649.

23. Cognigni F, Dinarelli S, Girasole M, Longo G, Fabi G, Rossi M. 3D X-ray Microscopy (XRM) investigation of exogenous materials inside mussels' organs. NanoInnovation. 2022;1265:012012.

24. BEAMIT, [Online]. Available: https://www.beam-it.eu/it/.

25. Object Research Systems (ORS) Inc., Dragonfly is the Premier Software Platform for Scientific Image Processing. Object Research Systems (ORS) Inc., 2023. [Online]. Available: https://theobjects.com/index.html.

26. Hanzl P, Zetek M, Bakša T, Kroupa T. The influence of processing parameters on the mechanical properties of SLM parts. Proc Eng. 2015;100:1405–13.

27. Shrestha S, Starr T, Chou K. A study of keyhole porosity in selective laser melting: single-track scanning with micro-CT analysis. J Manuf Sci Eng. 2019;141(7):071004.

28. Tan P, Kiran R, Zhou K. Effects of sub-atmospheric pressure on keyhole dynamics and porosity in products fabricated by selective laser melting. J Manuf Process. 2021;64:816–27.

29. Thijs L, Kempen K, Kruth J-P, Humbeeck JV. Fine-structured aluminium products with controllable texture by selective laser melting of pre-alloyed AlSi10Mg powder. Acta Mater. 2013;61(5):1809–19.

30. Pei W, Zhengying W, Zhen C, Jun D, Yuyang H, Junfeng L, Yatong Z. The AlSi10Mg samples produced by selective laser melting: single track, densification, microstructure and mechanical behavior. Appl Surf Sci. 2017;408:38–50.

31. Ricci S, Testa G, Iannitti G, Ruggiero A. Laser powder bed fusion of AlSi10Mg alloy: numerical investigation on the temperature field evolution. Forces Mech. 2022;8:100109.

32. Liu X, Zhao C, Zhou X, Shen Z, Liu W. Microstructure of selective laser melted AlSi10Mg alloy. Mater Methods. 2019;168:107677.

33. Jiang W, Yu W, Li J, You Z, Li C, Lv X. Segregation and morphological evolution of Si phase during electromagnetic directional solidification of hypereutectic Al-Si alloys. Materials. 2019;12(1):10.

34. Maskery I, Aboulkhair NT, Corfield MR, Tuck C, Clare AT, Leach RK, Wildman RD, Ashcroft IA, Hague RJM. Quantification and characterisation of porosity in selectively laser melted Al–Si10–Mg using X-ray computed tomography. Mater Charact. 2016;111:193–204.

35. Smith RJ, Hirsch M, Patel R, Li W, Clare AT, Sharples SD. Spatially resolved acoustic spectroscopy for selective laser melting. J Mater Process Technol. 2016;236:93–102.

36. Chen J, Hou W, Wang X, Chu S, Yang Z. Microstructure, porosity and mechanical properties of selective laser melted AlSi10Mg. Chin J Aeronaut. 2020;33(7):2043–54.

37. Hermanek P, Carmignato S. Porosity measurements by X-ray computed tomography: accuracy evaluation using a calibrated object. Precis Eng. 2017;49:377–87.

38. Zhu Y, Lin G, Khonsari MM, Zhang J, Yang H. Material characterization and lubricating behaviors of porous stainless steel fabricated by selective laser melting. J Mater Process Technol. 2018;262:41–52.

39. Santos LMS, Ferreira JAM, Jesus JS, Costa JM, Capela C. Fatigue behaviour of selective laser melting steel components. Theoret Appl Fract Mech. 2016;85:9–15.

40. Mathe NR, Tshabalala LC, Hoosain S, Motibane L, du Plessis A. The effect of porosity on the mechanical properties of Ti-6Al-4V components manufactured by high-power selective laser melting. Int J Adv Manuf Technol. 2021;115:3589–97.

41. Leuders S, Thöne M, Riemer A, Niendorf T, Tröster T, Richard HA, Maier HJ. On the mechanical behaviour of titanium alloy TiAl6V4 manufactured by selective laser melting: fatigue resistance and crack growth performance. Int J Fatigue. 2013;48:300–7.

42. Gong H, Rafi K, Gu H, Ram GDJ, Starr T, Stucker B. Influence of defects on mechanical properties of Ti–6Al–4 V components produced by selective laser melting and electron beam melting. Mater Des. 2015;86:545–54.

43. Siddique S, Imran M, Rauer M, Kaloudis M, Wycisk E, Emmelmann C, Walther F. Computed tomography for characterization of fatigue performance of selective laser melted parts. Mater Des. 2015;83:661–9.

44. Tillmann W, Schaak C, Nellesen J, Schaper M, Aydinöz ME, Hoyer KP. Hot isostatic pressing of IN718 components manufactured by selective laser melting. Addit Manuf. 2017;13:93–102.

45. Al-Maharma AY, Patil SP, Markert B. Effects of porosity on the mechanical properties of additively manufactured components: a critical review. Mater Res Exp. 2020;7:122001.

46. Lemaitre J. A course on damage mechanics. USA: Springer Science & Business Media; 2012.

47. Bonora N, Testa G, Ruggiero A, Iannitti G, Gentile D. Continuum damage mechanics modelling incorporating stress triaxiality effect on ductile damage initiation. Fatigue Fract Eng Mater Struct. 2020;43(8):1755–68.